Interfacial alloying contributions to the magnetic proximity effect in Pt/dysprosium iron garnet

Miela J. Gross [1], Javier Herrero-Martin [2], Sergio Valencia [3], Alexander J. Grutter [4], Julie A. Borchers [4], Yongseong Choi [5], Gilberto Fabbris [5], Allison C. Kaczmarek [6], Alexander E. Kossak [6], Jackson J. Bauer [6], Subhajit Kundu,[7] Supriya Ghosh,[7] K. Andre Mkhoyan [7], Angela Wittmann [8] and Caroline A. Ross [6,*]

[1]*Department of Electrical Engineering and Computer Science, Massachusetts Institute of Technology, Cambridge, Massachusetts 02139, USA*
[2]*ALBA Synchrotron Light Source, Cerdanyola del Vallés, Barcelona 08290, Spain*
[3]*Department of Spin and Topology in Quantum Materials, Helmholtz-Zentrum Berlin für Materialien und Energie, Berlin 12489, Germany*
[4]*NIST Center for Neutron Research, National Institute of Standards and Technology, Gaithersburg, Maryland 20899-6102, USA*
[5]*Advanced Photon Source, Argonne National Laboratory, Argonne, Illinois 60439, USA*
[6]*Department of Materials Science and Engineering, Massachusetts Institute of Technology, Cambridge, Massachusetts 02139, USA*
[7]*Department of Chemical Engineering and Materials Science, University of Minnesota, Minneapolis, Minnesota 55455, USA*
[8]*Institute of Physics, Johannes Gutenberg University Mainz, Mainz 55128, Germany*

(Received 27 January 2025; accepted 28 July 2025; published 13 August 2025)

The magnetic proximity effect (MPE), which describes a magnetic response from a heavy metal layer as a result of an adjacent magnetic layer, plays an important role in the behavior of heavy-metal/ferro- or ferrimagnet thin film heterostructures. However, in the case of heavy-metal/rare-earth iron garnet bilayers, the presence and magnitude of the MPE has been debated. We previously reported an MPE in a Pt/dysprosium iron garnet (DyIG) heterostructure where the two layers were grown without breaking vacuum, finding that the magnetic moment present in the Pt layer scales with the magnitude of the DyIG moment and varies nonmonotonically through the DyIG compensation temperature. However, the origin of the magnetic signal from the Pt layer was not identified. In contrast, Pt/DyIG grown with a vacuum break did not exhibit an MPE. Here we investigate the origin of the magnetic moment in the Pt layer using x-ray absorption spectroscopy, x-ray circular dichroism, composition mapping, and simulations of ion bombardment. The results are consistent with the presence of an intermixed Fe-Dy-Pt interfacial alloy layer formed during the growth of the Pt on the DyIG resulting in a measurable MPE.

DOI: 10.1103/7jdl-hkpp

I. INTRODUCTION

Heavy metal/magnetic insulator (HM/MI) heterostructures have become increasingly important in spintronics due to their utility in a broad range of devices including magnetic and magnetoelectric random access and racetrack memories [1–3]. These HM/MI interfaces enable spin transport, spin pumping, and spin-to-charge conversion phenomena [4–6], facilitating electrically controlled magnetization writing and readback. The insulating properties of MIs not only minimize power loss and Joule heating, but also often lead to low damping [7–11], which promotes fast switching dynamics and long-range magnon transport.

The magnetic proximity effect (MPE) describes magnetization of a normally nonmagnetic or paramagnetic material adjacent to a ferro- or ferrimagnetic metal or insulator, and it can manifest as anisotropic magnetoresistance or anomalous Hall or Nernst effects in the nonmagnetic material [12]. Based on electrical and x-ray measurements, an MPE has been identified in a variety of HM/magnet heterostructures including HMs Pt [13–17], Pd [18], Au [19], and W [20] interfaced with ferromagnetic transition metals [15,21,22], ferrimagnetic rare-earth–transition-metal alloys [23], spinels [24,25], and garnets [26–28]. Polarized neutron reflectometry (PNR) and x-ray magnetic circular dichroism (XMCD) have been used to quantify the magnetic moment arising from an MPE, but roughness, interdiffusion including interfacial alloying, and the small magnitude of the moment can complicate the interpretation of the measurements [29].

First-principles calculations show that an MPE is expected in Pt in intimate contact with a MI, for example in the first few planes of Pt atoms in $Pt/CoFe_2O_4$ [30] or across at least four atomic planes of Pt on YIG [31]. However, experimental evidence is more ambiguous. While MPE was reported in Pt/spinel [30] according to electrical measurements, several other reports of Pt/spinel [17,24,32] show no evidence of MPE in the Pt. There are reports of an MPE in Pt/YIG [16,33,34], Ta/YIG [27], and W/TmIG [28], but other experiments found no effect in similar heterostructures [33–35]. The structure and quality of the interface and the presence of interfacial contaminants or alloying have emerged as critical factors in determining the presence or absence of an MPE [29,31,36–39]. For example, Geprägs *et al.* showed that there was no MPE in Pt grown on top of YIG using evaporation, but growing YIG by pulsed laser deposition on top of Pt led to intermixing between YIG and Pt due to the high energy deposition process and there was a measurable MPE [36]. Vasili *et al.* [28] showed that an MPE was not present in $Pt/CoFe_2O_4$ when the Pt was deposited at room temperature,

*Contact author: caross@mit.edu

TABLE I. Samples used in this work. Superscripts I and E indicate *in situ* or *ex situ* growth of the capping layer.

Sample	Composition	Capping layer deposition	Ref.
$B1^I$	9 nm Pt/54 nm DyIG/GGG(111)	*In situ*, 100 °C	[40]
$B2^E$	9 nm Pt/54 nm DyIG/GGG(111)	*Ex situ*, 20 °C	[40]
$A1^I$	1.5 nm Pt/29 nm DyIG/GGG(111)	*In situ*, 20 °C	
$A2^I$	3 nm Pt/39 nm DyIG/GGG(111)	*In situ*, 20 °C	
$A3^E$	3 nm Pt/49 nm DyIG/GGG(111)	*Ex situ*, 20 °C	
$A4^E$	5 nm C/49 nm DyIG/GGG(111)	*Ex situ*, 20 °C	

but it existed when the Pt was grown at high temperature where intermixing was favored.

Previously, we reported an MPE in 9 nm Pt/42 nm dysprosium iron garnet ($Dy_3Fe_5O_{12}$, DyIG) grown on a $Gd_3Fe_5O_{12}$ (GGG) substrate in which the Pt/DyIG bilayer was grown sequentially without breaking vacuum ("*in situ*" growth) [40]. PNR measurements of the *in situ* sample taken across the compensation temperature of DyIG (220 K) indicated magnetization within the Pt layer that scaled with the magnetization of the DyIG. In contrast, a Pt/DyIG bilayer grown with a vacuum break between the deposition of the DyIG and Pt layers ("*ex situ*" growth) showed no magnetic signal from the Pt layer. Although PNR results of the *in situ* sample showed a magnetic moment in the Pt layer, negligible XMCD was observed at the Pt L_2 edge. We attributed the absence of a magnetic signature from Pt to the effects of averaging over the 9-nm-thick Pt layer, but it may also indicate that the magnetic moment arose from an element other than Pt. Therefore, the origin of the magnetic signal detected by PNR in Pt/DyIG remained unresolved. Here we further investigate the origin of the MPE by measuring XMCD of Pt/DyIG at the Fe $L_{2,3}$ edge. A magnetic signature attributed to metallic Fe suggests that a Pt-Fe-Dy dilute alloy created at the interface due to intermixing is responsible for the measured MPE, consistent with transport of ions in matter (TRIM) simulations [41].

II. METHODS

DyIG films of thickness 29–39 nm were grown on GGG substrates with (111) orientation using pulsed laser deposition (PLD), with a 248 nm KrF excimer laser at 10 Hz and a fluence of 2 J/cm^2. The stoichiometric DyIG target was made by solid oxide sintering methods [42]. An oxygen pressure of 150 mTorr (20 Pa) was maintained during substrate heating at 20 °C/min, film growth at 650 °C, and cooling at 20 °C/min. To make *in situ* samples, 1.5–3 nm Pt was sputtered onto the DyIG without breaking vacuum via an off-axis sputtering gun in the PLD chamber whose flux was oriented at 45° with respect to the sample plane. Sputtering was carried out at 20 °C substrate temperature and in 5 mTorr of argon with a dc power of 30 W/cm^2 over a 5-cm-diam target of 99.99% Pt metal (Kurt J. Lesker, Co.). The 20 °C sputtering process differs from that of our previous *in situ* sample of 9 nm Pt/42 nm DyIG/GGG(111) [40] (named here as sample $B1^I$) in which the Pt was sputtered when the DyIG/GGG(111) temperature had cooled to just below 100 °C. The resultant heterostructure geometries were as follows: sample $A1^I$: 1.5 nm Pt/29 nm DyIG/GGG(111) and sample $A2^I$: 3 nm Pt/39 nm DyIG/GGG(111). Additionally, we grew two 49 nm DyIG control samples on GGG(111) substrates during one PLD deposition. Sample $A4^E$ was DyIG capped *ex situ* with 5 nm carbon via electron beam evaporation, and sample $A3^E$ was DyIG coated with 3 nm of sputtered Pt *ex situ* after the PLD growth. The samples are summarized in Table I. The superscripts E and I represent *ex situ* and *in situ* capping of the DyIG respectively; samples A1–A4 were made for this study and samples B1 and B2 were described in [40].

High resolution x-ray diffraction (HRXRD) and x-ray reflectivity (XRR) data were collected using a Bruker K8 Discover diffractometer and a Rigaku Smartlab multipurpose diffractometer, both with a Cu $K\alpha$ x-ray source. Hysteresis loops were measured with a Digital Measurement Systems Vibrating Sample Magnetometer Model 1660 with a field applied in plane (IP) of the substrate. The PNR was measured at the NIST Center for Neutron Research with a polarized incident beam using the Polarized Beam Reflectometer and was analyzed using the Refl1D software package [43] to obtain a depth profile of the nuclear and magnetic scattering length densities (nSLD and mSLD, respectively). Uncertainties on fitted parameters were obtained using a Markov-chain Monte Carlo method as implemented in the DREAM algorithm of the BUMPS python package. STEM images and EDX elemental maps were collected using an aberration-corrected FEI Titan G2 60–300 STEM operated at 200 keV.

XAS and x-ray magnetic circular dichroism (XMCD) at the Pt L_2 edge were measured at the 4-ID-D beamline of the Advanced Photon Source at Argonne National Laboratory. The Pt L_2 XMCD data were taken at 10 K after the sample was field-cooled from 300 K in a $\pm$50 mT applied field. The Pt L_2 XMCD data were taken in fluorescence mode by monitoring Pt Lβ1 emission with an energy-dispersive detector. The incident x-ray angle was 0.275°, chosen to probe the whole Pt layer while minimizing the incident x-ray penetration into the DyIG/GGG(111) layers. The x-ray direction was parallel to the applied magnetic field, probing the IP Pt moment. The Pt L_2 edge was chosen instead of the Pt L_3 to avoid the overlap between the Pt $L\alpha$ emission (for the Pt L_3 edge) and the overwhelming Ga $K\alpha$ emission originating from the $Gd_3Ga_5O_{12}$ substrate. XAS and XMCD at the Pt M_3 and Fe $L_{2,3}$ edges were measured at beamline BL29 BOREAS of the ALBA Synchrotron Light Source in Barcelona, Spain.

III. RESULTS

We first discuss whether intermixing is predicted to occur during *in situ* growth due to bombardment by high energy species in the chamber. During typical sputter deposition conditions, the growing Pt film is bombarded both by Ar with

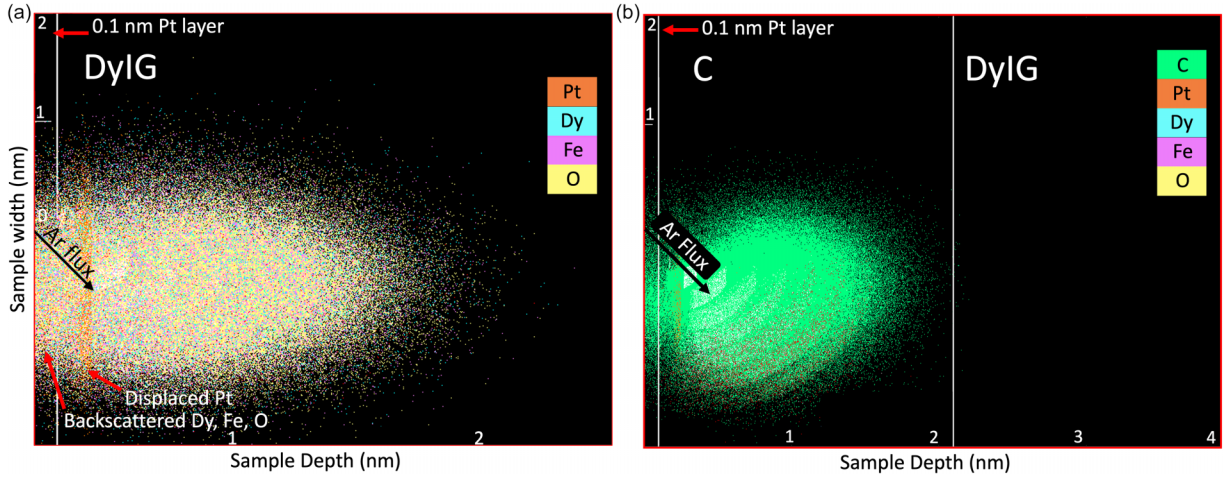

FIG. 1. TRIM depth profile of (a) 0.1 nm Pt/2.9 nm DyIG and (b) 0.1 nm Pt/2 nm C/1.9 nm DyIG after 10 000 Ar ions at 100 eV collided at 45° incidence into the sample surface. (b) TRIM depth profile of 0.1 nm Pt/2 nm C/1.9 nm DyIG after 20 000 Ar ions at 100 eV collided at 45° incidence into the sample surface. Individual displaced atoms are shown as colored dots: Pt (orange), Dy (blue), Fe (pink), O (yellow), C (green), and Ar (red).

energies up to 100s of eV and by Pt atoms with energies of a few eV to 10s of eV [44]. TRIM simulations [41,45] were used to model how Ar and Pt atoms at specified energies interact with a Pt-coated DyIG surface. Figure 1(a) shows the effect of bombardment of a DyIG surface covered with 0.1 nm of Pt by 100 eV Ar ions incident at 45°, corresponding to the off-axis sputter geometry. Bombardment by Ar leads to displacements of Pt from the surface layer up to 1.5 nm depth into the DyIG, as well as displacement of Dy, Fe, and O atoms from their sites in the crystal including backscattering into the surface Pt layer. In another simulation, bombardment by 30 eV Pt leads to implantation of Pt over 2 nm depth in the DyIG film. As the Pt film becomes thicker, it scatters and thermalizes the incoming energetic Pt and Ar species, reducing their interaction with the DyIG. Therefore, according to TRIM, when Pt is sputtered onto a clean DyIG surface, the incoming Ar and Pt have sufficient energy to promote intermixing near the interface, leading to incorporation of elements of the DyIG into the Pt. In contrast, Fig. 1(b), when the model includes a layer of 2 nm carbon between the DyIG and Pt (corresponding to the interface contamination in the *ex situ* samples $B2^E$ and $A3^E$), the collision cascade is mainly confined to the C layer, and the backscattering of Fe and other species into the Pt becomes negligible. Therefore, intermixing is suppressed if the garnet surface has been exposed to contamination by an adsorbed layer prior to sputtering.

We now turn to the magnetic and structural characterization of the samples, shown in Fig. 2. Hysteresis loops of samples $A1^I$ and $A2^I$ measured by VSM at room temperature with an in-plane field are shown in Fig. 2(a). The saturation magnetization is 30 ± 5 kA/m and 36 ± 5 kA/m, respectively, with a coercivity of order 1 mT, similar to samples $B1^I$ and $B2^E$ [40]. The magnetization is consistent with that of bulk DyIG, which has a modest magnetization of around 30 kA/m at room temperature. (The error of $\pm$ 5 kA/m is mainly caused by the large background signal of the substrate.) Any evidence of MPE would be below the detection limit of this measurement. Figure 2(b) shows the HRXRD of $A1^I$ and $A2^I$ around the (444) peak. Figures 2(c) and 2(d) present hysteresis loops and HRXRD from a sister sample of $A3^E$ and $A4^E$ consisting of 49 nm DyIG/GGG(111). The saturation magnetization is 38 ± 5 kA/m and coercivity on the order of 1 mT, similar to $A1^I$ and $A2^I$ despite the higher DyIG thickness. The HDXRD shows the same (444) peak position as $A1^I$ and $A2^I$ but closer-spaced Laue fringes due to the higher film thickness. The DyIG films are under in-plane compression due to epitaxial growth on the substrate because the DyIG lattice parameter exceeds that of GGG [46]. Considering the negative magnetostriction coefficient of DyIG, $\lambda_{111} = -5.9 \times 10^{-6}$ [47], both magnetoelastic and magnetostatic anisotropies favor an in-plane easy axis.

STEM-EDX elemental mapping, Fig. 3(a), was used to examine the Fe and Dy distribution in sample $B1^I$. Both Fe and Dy are clearly visualized in the DyIG. Weak signals from Dy and Fe are seen in the Pt layer. Elemental composition profiles, Fig. 3(b), provide supportive evidence for intermixing at the Pt garnet interface, indicating up to approximately 10 at.% Fe and 4 at.% Dy in the first few nm of the Pt layer. Similarly, in YIG/Pt [48], intermixing at the interface was revealed by electron energy loss spectroscopy. In contrast to Fig. 3(a), in *ex situ* garnet/Pt samples reported earlier [11], cross-sectional imaging showed a 2 nm noncrystalline interfacial layer consistent with carbon contamination from atmospheric exposure.

To clarify the role of Fe, Dy, and Pt in the MPE, we performed XMCD and XAS measurements of the Fe $L_{2,3}$, Dy $M_{4,5}$, Pt M_3, and O K edges at the ALBA beamline and Pt L_2 at the Argonne beamline. Fe $L_{2,3}$ was measured for samples $B1^I$, $A1^I$, $A2^I$, $A3^E$, and $A4^E$ at low temperature (15 K) and room temperature (300 K), and Pt was measured for samples $A1^I$ (L_2) and $A2^I$ (both L_2 and M_3). Data were acquired in total electron yield (TEY) and partial florescence yield (PFY) modes. We will focus on the TEY data to analyze material close to the surface of the samples.

XAS measurements of sample $A2^I$ show clear Pt L_2 absorption peaks in Fig. 4(a). However, the XMCD signal is at most 0.002 when the Pt L_2 XAS is normalized to 1. As a comparison, for a monolayer of Pt on Fe, Miwa *et al.* [49]

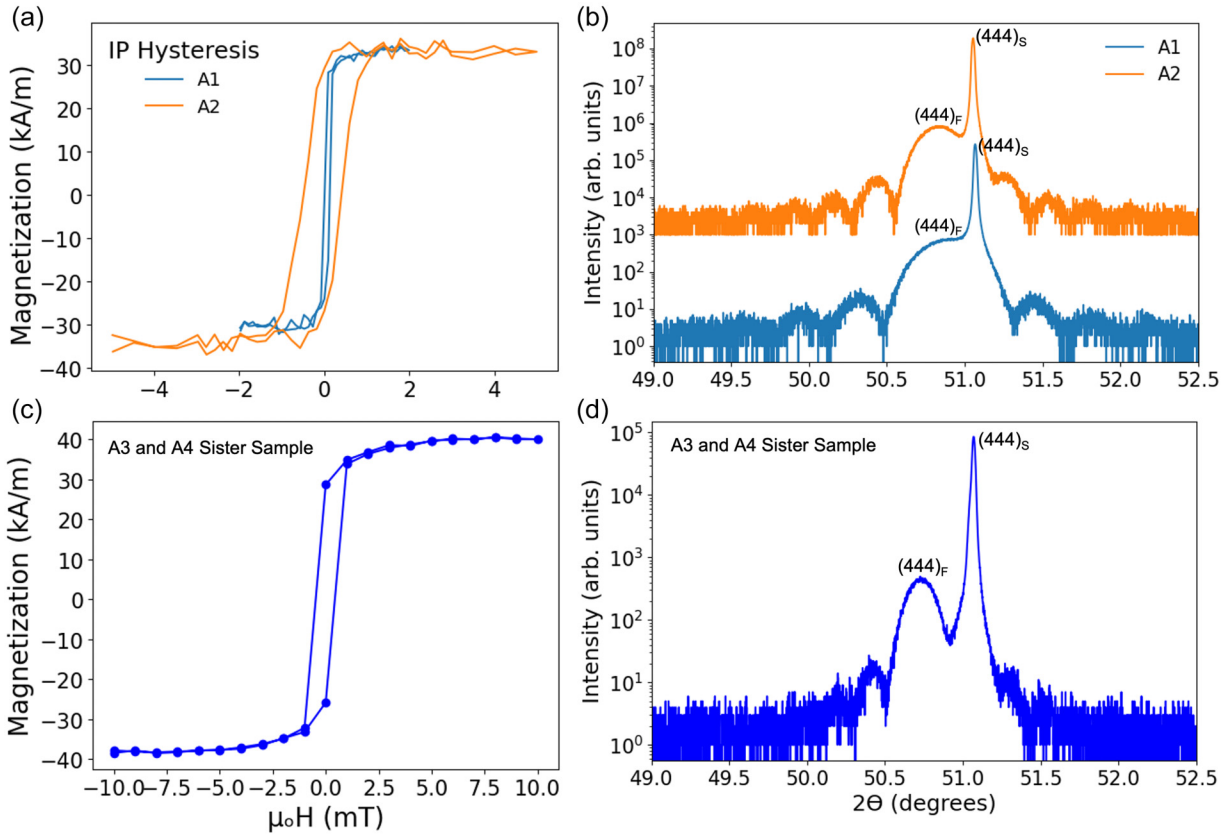

FIG. 2. Characterization of samples $A1^I$ [1.5 nm Pt/29 nm DyIG/GGG(111)], $A2^I$ [3 nm Pt/39 nm DyIG/GGG(111)], and a sister sample grown simultaneously with samples $A3^I$ and $A4^I$ consisting of 49 nm DyIG/GGG(111). Hysteresis loops of (a) $A1^I$, $A2^I$ and (c) sister sample of $A3^I$ and $A4^I$ taken with the external field applied in the film plane. HRXRD of (b) $A1^I$, $A2^I$ and (d) $A3^I$ and $A4^I$ sister sample at the (444) reflection with film peak and substrate peaks labeled with subscripts F and S, respectively. Curves have been shifted vertically for clarity.

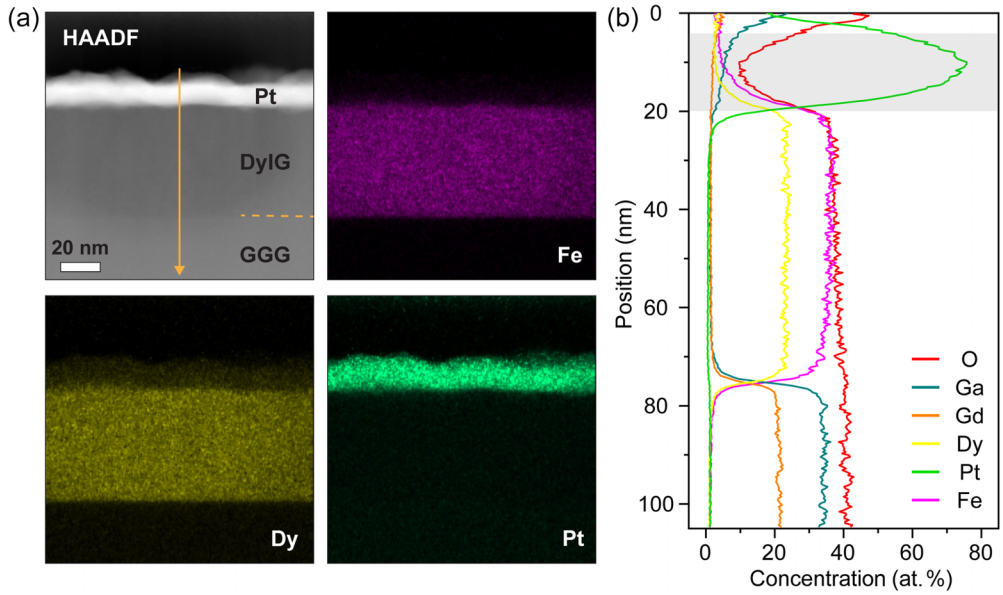

FIG. 3. (a) HAADF-STEM image and the corresponding EDX elemental maps from sample $B1^I$, adapted from supplementary information of [40]. The HAADF image shows the structure with the Pt layer above the DyIG. (b) Elemental distribution across the heterostructure from the linescan highlighted in the HAADF image in (a). The garnet/Pt interface corresponds to the lower boundary of the shaded region.

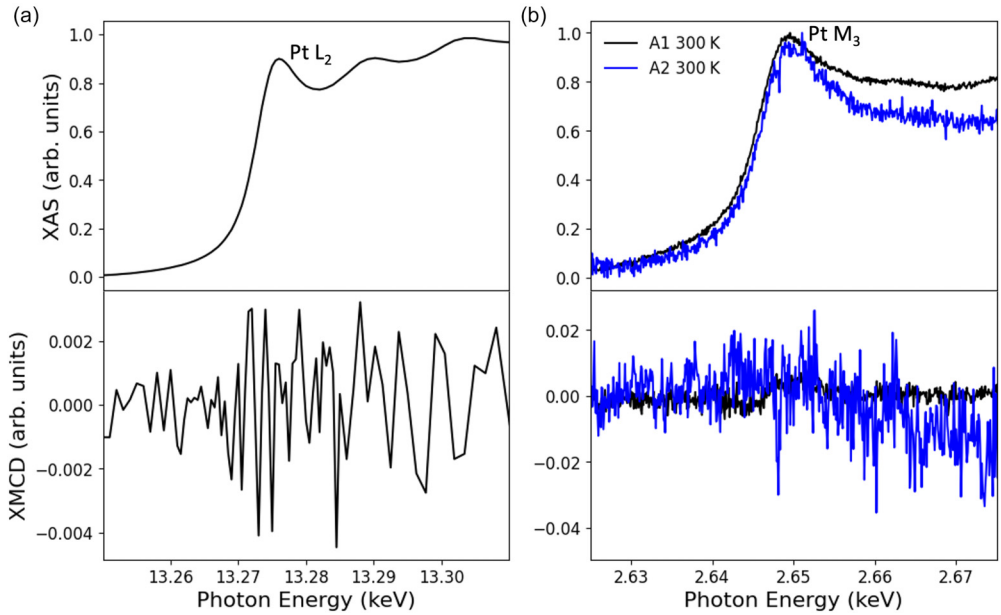

FIG. 4. (a) The Pt L_2 XAS and XMCD data of $A2^I$ taken at 10 K, field-cooled from 300 K with ± 50 mT applied IP. The Pt L_2 XAS and XMCD are normalized to the edge jump of 1. The difference between the two field directions is replotted as XMCD, to remove systematic artifacts. (b) Pt M_3 XAS and XMCD data of $A1^I$ (black) and $A2^I$ (blue) taken at 300 K and normalized for clarity.

showed Pt L_3 XMCD of 0.2 and Pt L_2 XMCD of 0.1 when normalized to the Pt L_3 edge jump of 2 and Pt L_2 edge jump of 1, respectively, corresponding to 0.355 μ_B/Pt via XMCD sum rules. Based on normalizing the Pt L_2 edge in the same manner, our Pt L_2 XMCD signal of 0.002 corresponds to at most 0.007 μ_B/Pt. Additionally, XAS and XMCD measurements of $A1^I$ and $A2^I$ at the Pt M_3 edge further confirm a negligible magnetic signal from Pt [Fig. 4(b)], similar to our past results for sample $B1^I$ at the Pt L_2 edge [40]. Thus, none of $A1^I$, $A2^I$, nor $B1^I$ indicate an MPE arising from the Pt. The electron escape depth in the TEY measurements is 1–5 nm, which exceeds the Pt thickness of samples $A1^I$ and $A2^I$. While any XMCD signal of the Pt near the interface in sample $B1^I$ may have been obscured due to the 9 nm thickness of the Pt, as proposed in [40], this is unlikely to explain a lack of Pt XMCD in $A1^I$ and $A2^I$ where the Pt is much thinner. These results suggest that the magnetic signal detected in the Pt layer by PNR in sample $B1^I$ originates from an element other than Pt. As a comparison, Lin *et al.* [50] reported an MPE in Pd/YIG based on electrical measurements, yet XMCD measurements in similar Pd/YIG stacks by d'Allivy Kelly *et al.* [51] did not show magnetism in the Pd.

We next consider whether the MPE might arise from Fe present in the Pt layer. Valence states and coordination of Fe were inferred from the peak positions of the $L_{2,3}$ absorption spectra [52]. Measurements at 300 K of Fe in samples $B1^I$ and $A1^I$ [Fig. 5(a)] show the L_3 peak around 709 eV and L_2 around 721 eV. The two samples were measured under identical beamline conditions, and the background and lower intensity of the Fe peaks from sample $B1^I$ is attributed to the reduced signal-to-noise ratio caused by its thicker Pt layer. All the samples show a main L_3 peak at 709 eV corresponding to tetrahedral Fe^{3+}, and a smaller peak at a lower energy (∼708 eV). The ∼708 eV peak in iron garnets as well as a higher energy shoulder is attributed to octahedral Fe^{2+} [42,45]. Octahedral Fe^{2+} is not unexpected, occurring as a result of oxygen deficiency or from charge transfer from Pt [42]. Analysis of terbium iron garnet (TbIG) and YIG films indicated Fe^{2+} concentrations of 5–10 % [44,42]. However, the 708 eV peak is significantly larger in sample $B1^I$ compared to $A1^I$, $A3^E$, and $A4^E$ [Fig. 5(c)] and to other garnets including YIG, EuIG, and TbIG [53–55], and is therefore unlikely to be solely due to Fe^{2+} in the garnet.

Metallic Fe also produces a peak at 707.9 eV [44]. We hypothesize that the large ∼708 eV peak in sample $B1^I$ arises from metallic Fe alloyed into the Pt layer during the sputtering of the Pt film. (The 3–5 nm escape depth and low signal-to-noise ratio of the XAS scan of $B1^I$ prevents a quantitative analysis of the metallic Fe content, but an estimate of 2–10 at.% is obtained from PNR, described below.) In comparison, Vasili *et al.* [29] reported the presence of metallic Fe and Co in $Pt/CoFe_2O_4$ films when the Pt was grown at an elevated temperature of 400 °C, favoring intermixing of Fe and Co into the Pt. Other works demonstrate structural changes at Pt/oxide interfaces, e.g., modification of YIG due to sputtering of Pt [56] and modification of the Pt microstructure by moderate heating [57]. If the enhanced 708 eV peak arises from intermixing in *in situ* grown bilayers, we may also expect to see it in sample $A1^I$, but this was not observed. The 1.5 nm Pt of sample $A1^I$ may be thin enough to allow for atmospheric oxidation of any metallic Fe that was incorporated into the Pt.

The Fe XMCD of $B1^I$ and $A1^I$ [Fig. 5(b)], $A3^E$ and $A4^E$ [Fig. 5(d)] indicates contributions of opposite sign for the tetrahedral and octahedral Fe^{3+} moments as expected for garnets [40]. Samples $A1^I$, $A3^E$, and $A4^E$ show little difference in the relative heights and positions of the Fe^{3+} XMCD peaks at 15 K compared to 300 K (orange and blue data). However, sample $B1^I$ shows a large increase in XMCD associated with the 708 eV peak at 15 K (purple data). This correlates with the

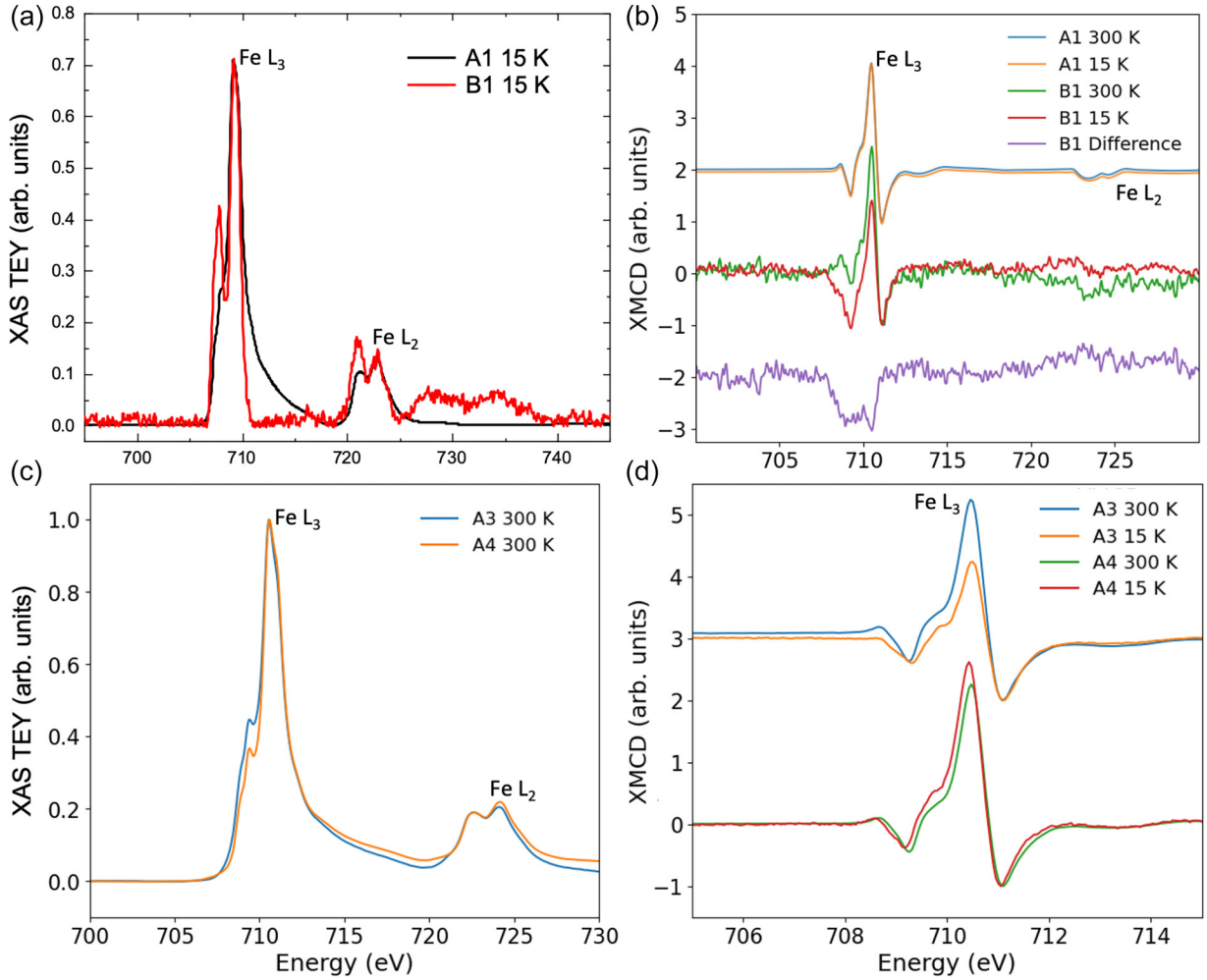

FIG. 5. X-ray absorption and circular dichroism data at the Fe L_3 edge. (a) XAS TEY data taken at 15 K of samples $A1^I$ (black) and $B1^I$ (red) with background subtraction. $B1^I$ shows a much stronger peak around 708 eV. (b) XMCD taken at 15 K (orange, red) and 300 K (blue, green) of samples $B1^I$ and $A1^I$ normalized to the 711 eV peak. The scans have been offset vertically for clarity. The data for $A1^I$ at 15 and 300 K (orange and blue) overlap almost exactly, whereas the data for $B1^I$ at 15 and 300 K (red and green) show a significant difference around the L_3 peak (purple). (c) XAS TEY data of the Fe L_3 edge at 300 K of $A3^E$ and $A4^E$ control samples. (d) XMCD data of $A3^E$ and $A4^E$ taken at 15 K (orange, red) and 300 K (blue, green) normalized at the 711 eV peak and shifted vertically for clarity.

increased MPE measured at low temperature by PNR [40] and suggests the MPE is associated with the presence of metallic Fe. The 708 eV peak indicates magnetization of the proposed metallic Fe antiparallel to the tetrahedral Fe^{3+}, i.e., parallel to the net DyIG moment below the compensation temperature.

Our previous analysis of the PNR data of sample $B1^I$ did not consider alloying of the Pt, which can raise the nSLD compared to that of bulk Pt. To examine the effects of interfacial alloying of Fe and Dy into the Pt, we reanalyzed the PNR data of sample $B1^I$ [40], adding a new interfacial layer to the model with relaxed constraints on its nSLD values. Any magnetization in the Pt layer is confined to this new interfacial layer, and there is no magnetic moment in the outer region of the Pt. This new model (Fig. 6) shows a better fit to the data, indicated by a χ^2 of 9.41, compared to our prior bilayer models [40] where the lowest χ^2 was 9.71. In the new trilayer model, the Pt layer and intermixed layer have fitted nSLD values of $6.205(10) \times 10^{-4}\,\mathrm{nm}^{-2}$ and $6.376(5) \times 10^{-4}\,\mathrm{nm}^{-2}$, respectively. Fe causes a greater change in nSLD of Pt compared to Dy [58]. Assuming that Fe dominates the change in nSLD, we may estimate the Fe-content in the intermixed layer by either comparing the raw nSLD values to the value for bulk Pt ($6.357 \times 10^{-4}\,\mathrm{nm}^{-2}$) or using the contrast between the intermixed and Pt layers. These methods give an approximate Fe content range of 2–10 at. % and hence 2.1–5 at. % Dy based on a 3:5 Dy:Fe ratio. The fitted thickness of the intermixed layer was approximately 4.3 nm.

The PNR data for sample $B1^I$ [40] indicated a positive MPE at 10 and 300 K, i.e., the magnetization in the Pt layer near the interface is parallel to that of the DyIG both above and below the compensation temperature of 220 K. Near the compensation temperature of the DyIG, the MPE was small or zero, but not negative. Our prior fit [40] yielded a moment per Pt atom at 10 K of $0.2-1\,\mu_B$/Pt depending on the thickness of the proximity-magnetized Pt layer used in the model. These values were large, exceeding those of $0.003-0.07\,\mu_B$/Pt reported elsewhere for Pt/YIG [33,35]. However, based on the new trilayer model proposed here (Fig. 6) and assuming the

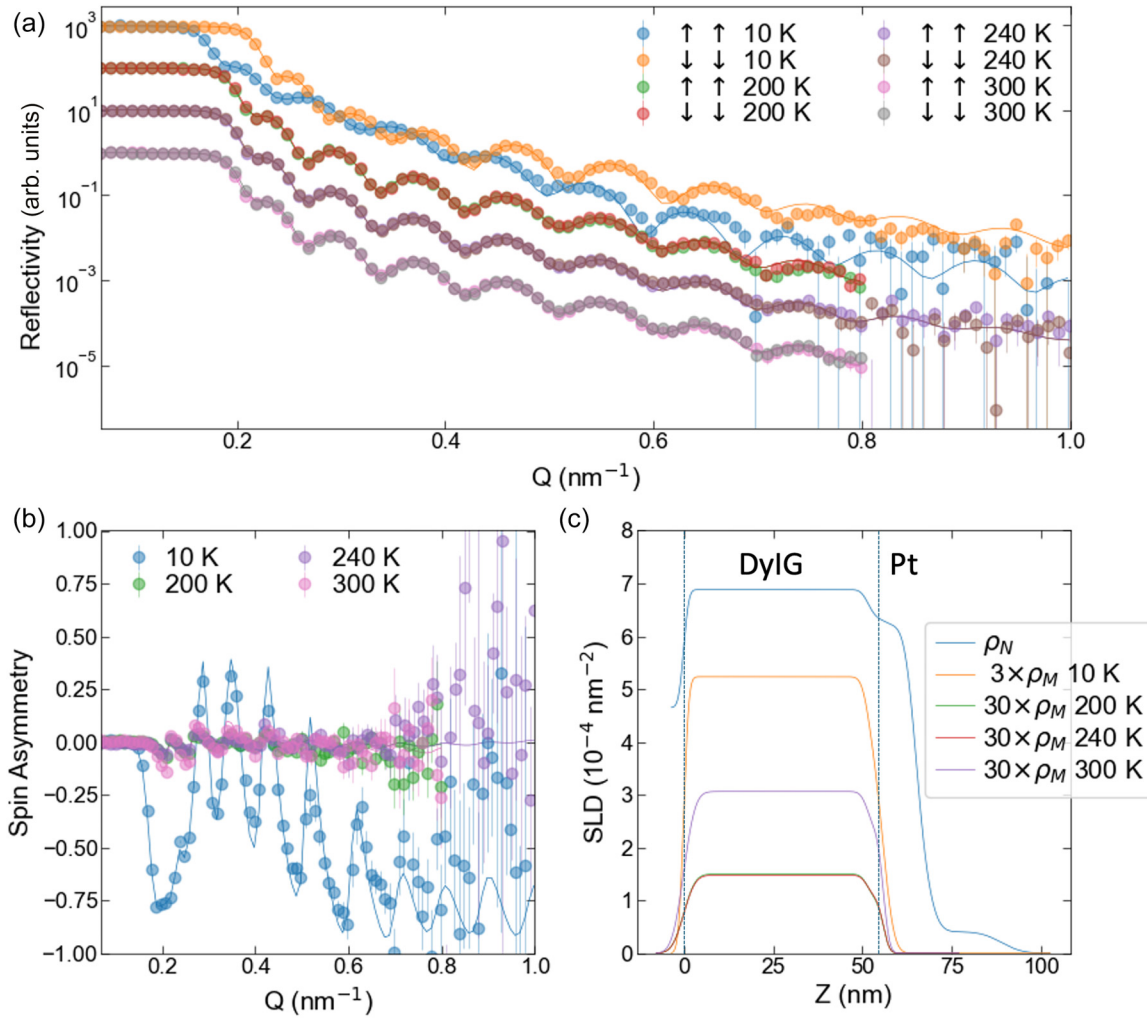

FIG. 6. Fit to the PNR results of sample B1^{I} incorporating an interfacial magnetic alloy layer. (a) PNR curves (data points) with fit (solid lines) vs scattering vector Q. Data and fits have been offset for clarity. (b) Spin asymmetry (data points) of the sample at 10, 200, 240, and 300 K alongside theoretical fits (solid lines). (c) Magnetic scattering length density (mSLD, ρ_M) at 10, 200, 240, and 300 K as well as nSLD (ρ_N, blue) vs depth Z. DyIG is present within the depth range of 0–54 nm, and the dashed lines designated the interface between the GGG substrate and DyIG as well as the boundary of the intermixed layer between the DyIG and Pt.

magnetization originates from the presence of 7 at. % Fe and 4.2 at. % Dy in the interfacial layer (near the middle of the estimated range), and taking the expected 10.6 μ_B/atom of metallic Dy, we obtain approximately 4.5 μ_B/Fe at 10 K in the interfacial layer.

The estimated magnetic moment attributed to Fe in this model may be compared with that of Pt-Fe alloys with low concentrations of Fe. Dilute Fe in Pt has a magnetic moment of 6.2 μ_B/Fe for Pt-0.87 at.% Fe and 5.2 μ_B/Fe for Pt-6.30 at.% Fe, with Curie temperatures of 5.4 and 104 K, respectively [59]. The moment/Fe atom in the dilute Pt-Fe alloys exceeds that of metallic Fe as a result of the mixing of Fe majority states with the Pt 4*d* valence states, where the Fe minority states form a virtual bound state above the Fermi level [60]. Furthermore, the magnetic moment of the Pt-Fe may persist above its Curie temperature due to exchange coupling from a neighboring magnetic layer, as seen in multilayers consisting of dilute Pt-Fe coupled to Co [61], where magnetization was present in the Pt-Fe even at room temperature for 6 at.% Fe. Coupling of the Pt-Fe to the net moment of DyIG in sample B1^{I} could analogously explain the presence of a magnetic moment in the Pt-Fe layer at room temperature but a weaker moment in Pt-Fe near the DyIG compensation temperature. We note also that Fe and Dy moments in the Pt could plausibly exhibit very different temperature dependencies.

The net magnetization of the interfacial Pt-Fe-Dy layer in sample B1^{I} is consistent with concentrations of $\leqslant$5 at.% Fe [59]. Equiatomic Fe-Pt alloys show a measurable induced polarization of the Pt [62,63]. However, the induced polarization of the Pt in our interfacial alloy would be near the beam line detection limit of 0.007 μ_B/Pt [15] and obscured by the large XAS signal from the nonalloyed part of the 9 nm film, explaining the lack of Pt XMCD.

The XAS, XMCD, and PNR data are therefore consistent with the hypothesis that the MPE observed in the Pt layer grown *in situ* on DyIG, sample B1^{I}, originates from a Fe-Dy-Pt interfacial alloy that developed by intermixing during the Pt growth. Several past reports have reached similar conclusions

in Pt/magnetic insulator stacks. While Lu *et al.* [33] reported an MPE in Pt atop YIG, Geprägs *et al.* [34] pointed out that the XMCD and XAS data of [33] were characteristic of an intermixed Pt film as the source of the MPE. Reports of MPE by Geprägs *et al.* [36], Vasili *et al.* [29], Miao *et al.* [26,64], and Kikkawa *et al.* [65] are consistent with interdiffusion. Schlitz *et al.* reported intermixing of Fe in a 2.5 nm interfacial region of Pt sputtered onto YIG [66]. The most critical requirement for intermixing is the clean interface between the Pt and DyIG enabled by the *in situ* growth process. This prevents the formation of a carbon-based contamination layer that acts as a barrier to intermixing as found with the *ex situ* growth process [40] and in the TRIM modeling. These results highlight the importance of the film preparation conditions on MPE and spin transport phenomena in HM/MI heterostructures.

IV. CONCLUSION

We investigated MPE in 1.5, 3, and 9 nm Pt/DyIG films (samples $A1^I$, $A2^I$, $B1^I$) grown *in situ* on GGG (111) substrates without a vacuum break between the DyIG and Pt depositions. TRIM simulations modeling the bombardment of Pt/DyIG by energetic sputtered Ar and Pt predict implantation of Pt into the DyIG within 1–2 nm from the interface and backscattering of Dy and Fe into the Pt. The presence of Dy and Fe in the Pt is consistent with STEM elemental mapping of the cross section of sample $B1^I$. XAS and XMCD measurements show that the magnetic signal detected by PNR in the Pt layer of $B1^I$ is consistent with the presence of metallic Fe within the Pt, rather than originating from polarization of the Pt itself. No magnetic moment was found in the Pt layer of samples $A1^I$ or $A2^I$, which is attributed to atmospheric oxidation of the Fe and/or a lesser amount of intermixing.

The magnetic moment of the interfacial alloy is fitted by PNR analysis. Considering a 4.3-nm-thick alloy of 7 at.% Fe and 4.2 at.% Dy adjacent to the DyIG, and taking the contribution of Dy as 10.6 μ_B/atom, we obtain a magnetization of 4.5 μ_B/Fe at 10 K. The magnetic moment of the alloy persists to high temperatures via exchange coupling to the DyIG layer. The interfacial alloy is formed under growth conditions that include a clean interface and energetic bombardment. These observations help explain the diverse reports of an MPE in HM/MI heterostructures due to the sensitivity of intermixing to growth conditions and the significant magnetic moment of dilute HM-Fe-RE alloys.

ACKNOWLEDGMENTS

M.J.G., A.E.K., and C.A.R. acknowledge the support of the National Science Foundation, Awards No. DMR 1808190 and No. ECCS 2152528 and the SMART Center, an NCORE Center of the Semiconductor Research Corporation. The x-ray experiments were performed at BL29 – BOREAS beamline at ALBA Synchrotron with the collaboration of the ALBA staff. The work performed at the Advanced Photon Source was supported by the U.S. Department of Energy, Office of Science, and Office of Basic Energy Sciences under Contract No. DE-AC02-06CH11357. S.K., S.G., and K.A.M. acknowledge support from the SMART Center, an NCORE Center of the Semiconductor Research Corporation. Parts of this work were carried out in the Characterization Facility, University of Minnesota, which receives partial support from the NSF through the MRSEC (Award No. DMR-2011401) and the NNCI (Award No. ECCS-2025124) programs. A.C.K. acknowledges support from the NSF Graduate Research Fellowship Program.

Certain commercial equipment, instruments, and materials are identified to specify adequately the experimental procedures. In no case does such identification imply recommendation or endorsement by the National Institute of Standards and Technology, nor does it imply that the materials or equipment identified are necessarily the best available for the purpose.

DATA AVAILABILITY

The data are available from the authors upon reasonable request.

[1] C. Chappert, A. Fert, and F. N. Van Dau, The emergence of spin electronics in data storage, Nat. Mater. **6**, 813 (2007).

[2] K. L. Wang, J. G. Alzate, and P. Khalili Amiri, Low-power non-volatile spintronic memory: STT-RAM and beyond, J. Phys. D **46**, 074003 (2013).

[3] Y. Zhang, X. Feng, Z. Zheng, Z. Zhang, K. Lin, X. Sun, G. Wang, J. Wang, J. Wei, P. Vallobra, Y. He, Z. Wang, L. Chen, K. Zhang, Y. Xu, and W. Zhao, Ferrimagnets for spintronic devices: From materials to applications, Appl. Phys. Rev. **10**, 011301 (2023).

[4] S. Vélez, J. Schaab, M. S. Wörnle, M. Müller, E. Gradauskaite, P. Welter, C. Gutgsell, C. Nistor, C. L. Degen, M. Trassin, M. Fiebig, and P. Gambardella, High-speed domain wall racetracks in a magnetic insulator, Nat. Commun. **10**, 4750 (2019).

[5] S. K. Kim, G. S. D. Beach, K. J. Lee, T. Ono, T. Rasing, and H. Yang, Ferrimagnetic spintronics, Nat. Mater. **21**, 24 (2022).

[6] Y. Kajiwara, K. Harii, S. Takahashi, J. Ohe, K. Uchida, M. Mizuguchi, H. Umezawa, H. Kawai, K. Ando, K. Takanashi, S. Maekawa, and E. Saitoh, Transmission of electrical signals by spin-wave interconversion in a magnetic insulator, Nature (London) **464**, 262 (2010).

[7] V. V. Kruglyak, S. O. Demokritov, and D. Grundler, Magnonics, J. Phys. D **43**, 260301 (2010).

[8] A. A. Serga, A. V. Chumak, and B. Hillebrands, YIG magnonics, J. Phys. D **43**, 264002 (2010).

[9] L. J. Cornelissen, J. Liu, R. A. Duine, J. Ben Youssef, and B. J. Van Wees, Long-distance transport of magnon spin information in a magnetic insulator at room temperature, Nat. Phys. **11**, 1022 (2015).

[10] T. Fakhrul, S. Tazlaru, B. Khurana, L. Beran, J. Bauer, M. Vančík, A. Marchese, E. Tsotsos, M. Kučera, Y. Zhang, M. Veis, and C. A. Ross, High figure of merit magneto-optical Ce- and Bi-substituted terbium iron garnet films integrated on Si, Adv. Opt. Mater. **9**, 2100512 (2021).

[11] L. Caretta, E. Rosenberg, F. Büttner, T. Fakhrul, P. Gargiani, M. Valvidares, Z. Chen, P. Reddy, D. A. Muller, C. A. Ross, and

G. S. D. Beach, Interfacial Dzyaloshinskii-Moriya interaction arising from rare-earth orbital magnetism in insulating magnetic oxides, Nat. Commun. **11**, 1090 (2020).

[12] J. J. Hauser, Magnetic proximity effect, Phys. Rev. **187**, 580 (1969).

[13] F. Wilhelm, P. Poulopoulos, G. Ceballos, H. Wende, K. Baberschke, P. Srivastava, D. Benea, H. Ebert, M. Angelakeris, N. K. Flevaris, D. Niarchos, A. Rogalev, and N. B. Brookes, Layer-resolved magnetic moments in Ni/Pt multilayers, Phys. Rev. Lett. **85**, 413 (2000).

[14] S. Ferrer, J. Alvarez, E. Lundgren, X. Torrelles, P. Fajardo, and F. Boscherini, Surface x-ray diffraction from ultrathin films and alloys: Structure and magnetism, Phys. Rev. B **56**, 9848 (1997).

[15] S. Rüegg, G. Schütz, P. Fischer, R. Wienke, W. B. Zeper, and H. Ebert, Spin-dependent x-ray absorption in Co/Pt multilayers, J. Appl. Phys. **69**, 5655 (1991).

[16] S. Y. Huang, X. Fan, D. Qu, Y. P. Chen, W. G. Wang, J. Wu, T. Y. Chen, J. Q. Xiao, and C. L. Chien, Transport magnetic proximity effects in platinum, Phys. Rev. Lett. **109**, 107204 (2012).

[17] T. Kuschel, C. Klewe, J. M. Schmalhorst, F. Bertram, O. Kuschel, T. Schemme, J. Wollschläger, S. Francoual, J. Strempfer, A. Gupta, M. Meinert, G. Götz, D. Meier, and G. Reiss, Static magnetic proximity effect in $Pt/NiFe_2O_4$ and Pt/Fe bilayers investigated by X-ray resonant magnetic reflectivity, Phys. Rev. Lett. **115**, 097401 (2015).

[18] J. Vogel, A. Fontaine, V. Gros, F. Petroff, J. P. Kappler, G. Krill, A. Rogalev, and J. Goulon, Structure and magnetism of Pd in Pd/Fe multilayers studied by XMCD at the Pd $L_{2,3}$ edges, J. Phys. IV France **7**, C2-401 (1997).

[19] F. Wilhelm, M. Angelakeris, N. Jaouen, P. Poulopoulos, E. T. Papaioannou, C. Mueller, P. Fumagalli, A. Rogalev, and N. K. Flevaris, Magnetic moment of Au at Au/Co interfaces: A direct experimental determination, Phys. Rev. B **69**, 220404 (2004).

[20] F. Wilhelm, P. Poulopoulos, A. Scherz, H. Wende, K. Baberschke, M. Angelakeris, N. K. Flevaris, J. Goulon, and A. Rogalev, Interface magnetism in 3*d*/5*d* multilayers probed by X-ray magnetic circular dichroism, Phys. Status Solidi A **196**, 33 (2003).

[21] F. Wilhelm, P. Poulopoulos, H. Wende, A. Scherz, K. Baberschke, M. Angelakeris, N. K. Flevaris, and A. Rogalev, Systematics of the induced magnetic moments in 5*d* layers and the violation of the third Hund's rule, Phys. Rev. Lett. **87**, 207202 (2001).

[22] R. Tyer, G. Van der Laan, W. M. Temmermann, Z. Szotek, F. Wilhelm, P. Poulopoulos, H. Wende, A. Scherz, K. Baberschke, M. Angelakeris, N. K. Flevaris, and A. Rogalev, Comment on "systematics of the induced magnetic moments in 5*d* layers and the violation of the third Hund's rule" (multiple letters), Phys. Rev. Lett. **90**, 129701 (2003).

[23] C. Swindells, B. Nicholson, O. Inyang, Y. Choi, T. Hase, and D. Atkinson, Proximity-induced magnetism in Pt layered with rare-earth-transition-metal ferrimagnetic alloys, Phys. Rev. Res. **2**, 033280 (2020).

[24] M. Collet, R. Mattana, J. B. Moussy, K. Ollefs, S. Collin, C. Deranlot, A. Anane, V. Cros, F. Petroff, F. Wilhelm, and A. Rogalev, Investigating magnetic proximity effects at ferrite/Pt interfaces, Appl. Phys. Lett. **111**, 202401 (2017).

[25] T. Kikkawa, M. Suzuki, R. Ramos, M. H. Aguirre, J. Okabayashi, K. Uchida, I. Lucas, A. Anadón, D. Kikuchi, P. A. Algarabel, L. Morellón, M. R. Ibarra, and E. Saitoh, Interfacial ferromagnetism and atomic structures in high-temperature grown $Fe_3O_4/Pt/Fe_3O_4$ epitaxial trilayers, J. Appl. Phys. **126**, 143903 (2019).

[26] B. F. Miao, S. Y. Huang, D. Qu, and C. L. Chien, Physical origins of the new magnetoresistance in Pt/YIG, Phys. Rev. Lett. **112**, 236601 (2014).

[27] Y. Yang, B. Wu, K. Yao, S. Shannigrahi, B. Zong, and Y. Wu, Investigation of magnetic proximity effect in Ta/YIG bilayer Hall bar structure, J. Appl. Phys. **115**, 17C509 (2014).

[28] Q. Shao, A. Grutter, Y. Liu, G. Yu, C. Y. Yang, D. A. Gilbert, E. Arenholz, P. Shafer, X. Che, C. Tang, M. Aldosary, A. Navabi, Q. L. He, B. J. Kirby, J. Shi, and K. L. Wang, Exploring interfacial exchange coupling and sublattice effect in heavy metal/ferrimagnetic insulator heterostructures using Hall measurements, x-ray magnetic circular dichroism, and neutron reflectometry, Phys. Rev. B **99**, 104401 (2019).

[29] H. B. Vasili, M. Gamino, J. Gàzquez, F. Sánchez, M. Valvidares, P. Gargiani, E. Pellegrin, and J. Fontcuberta, Magnetoresistance in hybrid $Pt/CoFe_2O_4$ bilayers controlled by competing spin accumulation and interfacial chemical reconstruction, ACS Appl. Mater. Interfaces **10**, 12031 (2018).

[30] W. Amamou, I. V. Pinchuk, A. H. Trout, R. E. A. Williams, N. Antolin, A. Goad, D. J. O'Hara, A. S. Ahmed, W. Windl, D. W. McComb, and R. K. Kawakami, Magnetic proximity effect in $Pt/CoFe_2O_4$ bilayers, Phys. Rev. Mater. **2**, 011401 (2018).

[31] X. Liang, Y. Zhu, B. Peng, L. Deng, J. Xie, H. Lu, M. Wu, and L. Bi, Influence of interface structure on magnetic proximity effect in $Pt/Y_3Fe_5O_{12}$ heterostructures, ACS Appl. Mater. Interfaces **8**, 8175 (2016).

[32] M. Valvidares, N. Dix, M. Isasa, K. Ollefs, F. Wilhelm, A. Rogalev, F. Sánchez, E. Pellegrin, A. Bedoya-Pinto, P. Gargiani, L. E. Hueso, F. Casanova, and J. Fontcuberta, Absence of magnetic proximity effects in magnetoresistive $Pt/CoFe_2O_4$ hybrid interfaces, Phys. Rev. B **93**, 214415 (2016).

[33] Y. M. Lu, Y. Choi, C. M. Ortega, X. M. Cheng, J. W. Cai, S. Y. Huang, L. Sun, and C. L. Chien, Pt magnetic polarization on $Y_3Fe_5O_{12}$ and magnetotransport characteristics, Phys. Rev. Lett. **110**, 147207 (2013).

[34] S. Geprägs, S. T. B. Goennenwein, M. Schneider, F. Wilhelm, K. Ollefs, A. Rogalev, M. Opel, and R. Gross, Comment on "Pt magnetic polarization on $Y_3Fe_5O_{12}$ and magnetotransport characteristics", arXiv:1307.4869.

[35] S. Geprägs, S. Meyer, S. Altmannshofer, M. Opel, F. Wilhelm, A. Rogalev, R. Gross, and S. T. B. Goennenwein, Investigation of induced Pt magnetic polarization in $Pt/Y_3Fe_5O_{12}$ bilayers, Appl. Phys. Lett. **101**, 262407 (2012).

[36] S. Geprägs, C. Klewe, S. Meyer, D. Graulich, F. Schade, M. Schneider, S. Francoual, S. P. Collins, K. Ollefs, F. Wilhelm, A. Rogalev, Y. Joly, S. T. B. Goennenwein, M. Opel, T. Kuschel, and R. Gross, Static magnetic proximity effects and spin Hall magnetoresistance in $Pt/Y_3Fe_5O_{12}$ and inverted $Y_3Fe_5O_{12}/Pt$ bilayers, Phys. Rev. B **102**, 214438 (2020).

[37] C. O. Avci, A. Quindeau, M. Mann, C. F. Pai, C. A. Ross, and G. S. D. Beach, Spin transport in as-grown and annealed thulium iron garnet/platinum bilayers with perpendicular magnetic anisotropy, Phys. Rev. B **95**, 115428 (2017).

[38] M. B. Jungfleisch, V. Lauer, R. Neb, A. V. Chumak, and B. Hillebrands, Improvement of the yttrium iron garnet/platinum

interface for spin pumping-based applications, Appl. Phys. Lett. **103**, 022411 (2013).

[39] J. Fontcuberta, H. B. Vasili, J. Gàzquez, and F. Casanova, On the role of interfaces on spin transport in magnetic insulator/normal metal heterostructures, Adv. Mater. Interfaces **6**, 1900475 (2019).

[40] J. J. Bauer, P. Quarterman, A. J. Grutter, B. Khurana, S. Kundu, K. A. Mkhoyan, J. A. Borchers, and C. A. Ross, Magnetic proximity effect in magnetic-insulator/heavy-metal heterostructures across the compensation temperature, Phys. Rev. B **104**, 094403 (2021).

[41] J. F. Ziegler, M. D. Ziegler, and J. P. Biersack, SRIM - The stopping and range of ions in matter (2010), Nucl. Instrum. Methods Phys. Res. B **268**, 1818 (2010).

[42] T. Goto, M. C. Onbaşlò, and C. A. Ross, Magneto-optical properties of cerium substituted yttrium iron garnet films with reduced thermal budget for monolithic photonic integrated circuits, Opt. Express **20**, 28507 (2012).

[43] B. J. Kirby, P. A. Kienzle, B. B. Maranville, N. F. Berk, J. Krycka, F. Heinrich, and C. F. Majkrzak, Phase-sensitive specular neutron reflectometry for imaging the nanometer scale composition depth profile of thin-film materials, Curr. Opin. Colloid Interface Sci. **17**, 44 (2012).

[44] J. Lu and C. G. Lee, Numerical estimates for energy of sputtered target atoms and reflected Ar neutrals in sputter processes, Vacuum **86**, 1134 (2012).

[45] S. J. Tan, W. Zhang, L. Yang, Y. Zhou, F. Jiao, W. Shi, and Z. Wang, Threshold displacement energy of lattice atoms in yttrium ion garnet, an ab initio molecular dynamics study, Chem. Phys. Lett. **771**, 138518 (2021).

[46] J. J. Bauer, E. R. Rosenberg, and C. A. Ross, Perpendicular magnetic anisotropy and spin mixing conductance in polycrystalline europium iron garnet thin films, Appl. Phys. Lett. **114**, 052403 (2019).

[47] S. Iida, Magnetostriction constants of rare earth iron garnets, J. Phys. Soc. Jpn. **22**, 1201 (1967).

[48] E. J. Guo, J. Cramer, A. Kehlberger, C. A. Ferguson, D. A. MacLaren, G. Jakob, and M. Kläui, Influence of thickness and interface on the low-temperature enhancement of the spin seebeck effect in YIG films, Phys. Rev. X **6**, 031012 (2016).

[49] S. Miwa, M. Suzuki, M. Tsujikawa, K. Matsuda, T. Nozaki, K. Tanaka, T. Tsukahara, K. Nawaoka, M. Goto, Y. Kotani, T. Ohkubo, F. Bonell, E. Tamura, K. Hono, T. Nakamura, M. Shirai, S. Yuasa, and Y. Suzuki, Voltage controlled interfacial magnetism through platinum orbits, Nat. Commun. **8**, 15848 (2017).

[50] T. Lin, C. Tang, H. M. Alyahayaei, and J. Shi, Experimental investigation of the nature of the magnetoresistance effects in Pd-YIG hybrid structures, Phys. Rev. Lett. **113**, 037203 (2014).

[51] O. D'Allivy Kelly, M. Collet, E. Jacquet, R. Mattana, F. Petroff, P. Bortolotti, V. Cros, A. Anane, F. Wilhelm, K. Ollefs, and A. Rogalev, Magnetic proximity effect free spin Hall magnetoresistance in YIG/Pd, Spin **7**, 1740005 (2017).

[52] G. Van Der Laan and I. W. Kirkman, The 2p absorption spectra of 3d transition metal compounds in tetrahedral and octahedral symmetry, J. Phys. Condens. Matter **4**, 4189 (1992).

[53] Y. Y. Chin, H. J. Lin, Y. F. Liao, W. C. Wang, P. Wang, D. Wu, A. Singh, H. Y. Huang, Y. Y. Chu, D. J. Huang, K. D. Tsuei, C. T. Chen, A. Tanaka, and A. Chainani, Local spin moments, valency, and long-range magnetic order in monocrystalline and ultrathin films of $Y_3Fe_5O_{12}$ garnet, Phys. Rev. B **99**, 184407 (2019).

[54] M. X. Guo, C. K. Cheng, Y. C. Liu, C. N. Wu, W. N. Chen, T. Y. Chen, C. T. Wu, C. H. Hsu, S. Q. Zhou, C. F. Chang, L. H. Tjeng, S. F. Lee, C. F. Pai, M. Hong, and J. Kwo, Single-crystal epitaxial europium iron garnet films with strain-induced perpendicular magnetic anisotropy: Structural, strain, magnetic, and spin transport properties, Phys. Rev. Mater. **6**, 054412 (2022).

[55] E. Rosenberg, J. Bauer, E. Cho, A. Kumar, J. Pelliciari, C. A. Occhialini, S. Ning, A. Kaczmarek, R. Rosenberg, J. W. Freeland, Y. Chen, J. Wang, J. LeBeau, R. Comin, F. M. F. de Groot, and C. A. Ross, Revealing site occupancy in a complex oxide: Terbium iron garnet, Small **19**, 2300824 (2023).

[56] D. Song, L. Ma, S. Zhou, and J. Zhu, Oxygen deficiency induced deterioration in microstructure and magnetic properties at $Y_3Fe_5O_{12}$/Pt interface, Appl. Phys. Lett. **107**, 042401 (2015).

[57] M. Isasa, A. Bedoya-Pinto, S. Vélez, F. Golmar, F. Sánchez, L. E. Hueso, J. Fontcuberta, and F. Casanova, Spin Hall magnetoresistance at Pt/$CoFe_2O_4$ interfaces and texture effects, Appl. Phys. Lett. **105**, 142402 (2014).

[58] NCNR, Neutron Activation and Scattering Calculator, https://www.ncnr.nist.gov/resources/activation/.

[59] J. Crangle and W. R. Scott, Dilute ferromagnetic alloys, J. Appl. Phys. **36**, 921 (1965).

[60] J. F. van Acker, P. J. W. Weijs, J. C. Fuggle, K. Horn, H. Haak, and K. H. J. Buschow, Photoemission investigation of the electronic structure of Fe-Pd and Fe-Pt alloys, Phys. Rev. B **43**, 8903 (1991).

[61] Q. L. Lv, J. W. Cai, S. L. He, and L. Sun, Perpendicular magnetic anisotropy and magnetic proximity effect in $Pt_{1-\delta}Fe_\delta$/Co multilayer films, J. Magn. Magn. Mater. **323**, 465 (2011).

[62] A. I. Figueroa, J. Bartolomé, L. M. García, F. Bartolomé, O. Bunău, J. Stankiewicz, L. Ruiz, J. M. González-Calbet, F. Petroff, C. Deranlot, S. Pascarelli, P. Bencok, N. B. Brookes, F. Wilhelm, A. Smekhova, and A. Rogalev, Structural and magnetic properties of granular Co-Pt multilayers with perpendicular magnetic anisotropy, Phys. Rev. B **90**, 174421 (2014).

[63] J. Honolka, T. Y. Lee, K. Kuhnke, A. Enders, R. Skomski, S. Bornemann, S. Mankovsky, J. Minár, J. Staunton, H. Ebert, M. Hessler, K. Fauth, G. Schütz, A. Buchsbaum, M. Schmid, P. Varga, and K. Kern, Magnetism of FePt surface alloys, Phys. Rev. Lett. **102**, 067207 (2009).

[64] B. F. Miao, L. Sun, D. Wu, C. L. Chien, and H. F. Ding, Magnetic scattering and spin-orbit coupling induced magnetoresistance in nonmagnetic heavy metal and magnetic insulator bilayer systems, Phys. Rev. B **94**, 174430 (2016).

[65] T. Kikkawa, M. Suzuki, J. Okabayashi, K. I. Uchida, D. Kikuchi, Z. Qiu, and E. Saitoh, Detection of induced paramagnetic moments in Pt on $Y_3Fe_5O_{12}$ via x-ray magnetic circular dichroism, Phys. Rev. B **95**, 214416 (2017).

[66] R. Schlitz, S. Granovsky, D. Pohl, A. Thomas, B. Rellinghaus, and S. T. B. Goennenwein, Nonlocal magnon-based transport in yttrium-iron-garnet-platinum heterostructures at high temperatures, Phys. Rev. B **103**, 214434 (2021).